Microstructure and Tribological Response of Selective Laser Melted AISI 316L Stainless Steel: The Role of Severe Surface Deformation

Vikesh Kumar[1], Manoj D. Joshi[1], Catalin Pruncu[3,4], Indrasen Singh[2], Santosh S. Hosmani[1]*

[1] Department of Metallurgy Engineering and Materials Science, Indian Institute of Technology Indore, Indore 453552, India

[2] Department of Mechanical Engineering, Indian Institute of Technology Indore, Indore 453552, India

[3] Design, Manufacturing & Engineering Management, University of Strathclyde, Glasgow, G1 1XJ, Scotland, UK

[4] Department of Mechanical Engineering, Imperial College London, Exhibition Rd., SW7 2AZ, London, UK

[*] Corresponding author: Tel.: 0731-660333 (Ext. 3243);

Contact e-mail: sshosmani@iiti.ac.in

Submitted: 17 December 2020 / Revised: 5 February 2021 / Accepted: 16 February 2021 / Published online:
Special Issue
JMEP-20-12-22476

[Additional Information]This invited article is part of a special topical focus in the *Journal of Materials Engineering and Performance* on Additive Manufacturing. The issue was organized by Dr. William Frazier, Pilgrim Consulting, LLC; Mr. Rick Russell, NASA; Dr. Yan Lu, NIST; Dr. Brandon D. Ribic, America Makes; and Caroline Vail, NSWC Carderock.

Abstract -

This study investigates the effect of surface mechanical attrition treatment (SMAT) (a severe surface-deformation process) on microstructure and tribological behaviour of AISI 316L steel samples manufactured using the selective laser melting (SLM) technique. The specimens are built in different directions (0°, 45°, and 90°). The microstructure of annealed SLM samples shows the non-uniform distribution and random orientation of grains. It contains high angle grain boundaries and a high density of dislocations. The average grain size is about 63, 51, and 41 μm for 0°, 45°, and 90° build direction, respectively. SMAT is beneficial for SLM steel to reduce surface roughness (by ~87%) and eliminate internal porosity. The deformed layer of SLM steel shows a highly dense network of slip bands,

distortion of grains, and hardness gradient (up to the depth of about 600 μm). Increase in surface hardness due to SMAT is maximum (~54%) for the sample having 90° build direction. Typical observation of deformation-induced martensite is absent for the SMAT processed SLM steel. Under the higher load (especially, 20 N), the tribological response of sample manufactured in 90° direction is superior amongst the non-treated samples. Severe surface deformation enhances the wear resistance and reduces the COF of SLM steel.

Keywords: SMAT; SLM; Wear; AISI 316L; Surface Nanostructuring

1. Introduction

Stainless steels are known for their superior mechanical characteristics. Amongst all grades of stainless steels, AISI 316L steel has an outstanding combination of corrosion resistance and mechanical properties. Such combination leads to its utilization in numerous aircraft components, medical implants, and petrochemical industries [1-3]. An advanced manufacturing technique called 'selective laser melting (SLM)' is becoming popular in various industrial platforms for designing and fabrication of machine components. A high degree of freedom in geometry, minimal wastage of material, superior mechanical strength, and faster manufacturing (as compared to the conventional route) are some of its plausible trademarks [4,5]. SLM is a powder-based additive manufacturing process. In this process, components are fabricated by driving the high power laser to cause a fusion of metal powder in a layer-by-layer architecture using CAD platform [6]. In the SLM process, product quality strongly depends on process parameters such as laser power, a layer thickness of powder bed, scanning speed, build direction, etc. [7,8]. High cooling rate (~10^5-10^7 $K \cdot s^{-1}$) in SLM technique induces a non-uniform microstructure (unlike the conventional casting and hot-/cold- rolled material) [9,10]. SLM 316L steel possesses grains with cellular dendrite and columnar structures, and grain size is in the range of 10–100 μm [11,12]. The hardness of SLM 316L stainless steel is typically higher than conventionally

manufactured 316L stainless steel [13]. Higher hardness of the steel is attributed to its fine grains and higher dislocation density [12].

High hardness of SLM 316L steel trigger about 28% lower wear rate as compared to the cast steel [14]. Many former studies on SLM technique explain the role of process parameters on internal defects and surface roughness of the 3D printed materials [15,16]. However, porosity and high surface roughness are still challenging to make this technique more powerful and economical. These drawbacks can adversely affect the wear resistance because they increase the probability of crack formation/propagation, resulting in material loss during dry sliding operation [11,17]. Various techniques are attempted to overcome these challenges. Laser surface re-melting can eliminate the porosity and minimize the surface roughness (for example, reduction in R_a from 12 μm to 1.5 μm) of the SLM steel, which in turn improves the fatigue resistance [18-20]. However, multiple laser scanning increases production cost and time significantly. Heat treatment can also decrease the internal porosity of the material to some extent; however, it significantly compromises the hardness of SLM steel [11]. Optimization of laser parameters, laser polishing, and electrochemical polishing are some of the approaches used to improve the surface finish of the SLM materials, where the most attainable surface roughness was 0.8 μm [7,8,19,21,22]. The ultrasonic nanocrystalline surface modification (UNSM) can eliminate the voids/porosity in the surface of the SLM 316L stainless steel [23]. Therefore, severe plastic deformation (SPD) is a promising route to eliminate internal defects, and hence, improve the mechanical properties of the SLM steel.

Surface mechanical attrition treatment (SMAT) is one of the SPD processes used for surface modification of conventionally manufactured metals/alloys. It was introduced by K. Lu and J. Lu in 1999 [24]. SMAT process involves strong impacts of balls (typically, 1-6 mm diameter), moving in random directions, on the surface specimen, which introduce a significantly high strain-rate (of the order of 10^3–10^5 s^{-1}) on the surface [25]. In case of conventionally manufactured steels, SMAT forms a gradient microstructure up to the depth of 200-300 μm (depending on the operating parameters such

as the number of balls, treatment time, ball speed, and ball diameter) [24,26]. Grain refinement, the formation of high dislocation density, phase transformations, and generation of shear-bands occur in the severely deformed layer of steels, depending on the stacking fault energy (SFE) of material [26-29]. SMAT is a capable process to enhance various properties of metallic materials such as hardness, strength, corrosion resistance, and wear resistance [25,26,28].

The current study aims to investigate the effect of build direction during SLM process and severe surface deformation on the microstructure, porosity, hardness, and tribological response of AISI 316L stainless steel. The microstructure of heat-treated/annealed and severely surface deformed SLM steel is investigated using an optical microscope, scanning electron microscope (SEM), electron backscatter diffraction (EBSD), and nanoindentation methods. Ball-on-disc type dry reciprocating wear test is conducted to study the tribological behaviour of the steel.

2. Materials and methods

A cylindrical disc of 5 mm thickness and 50 mm diameter was additively manufactured (by Incredible Additive Manufacturing Pvt. Ltd., Pune) using Renishaw AM 400 Laser Melting machine. Table 1 shows the chemical composition of AISI 316L stainless steel powder used to make the samples. Size of the powder particles was in the range of 15–45 μm. The laser scanning was carried out in argon atmosphere using 200 W laser power, 50 μm thick powder bed (layer), 110 μm hatch distance, 70-120 μm point distance, 80-120 μs exposure time, and 70 μm diameter of laser focus/spot. Figure 1 shows the three scanning strategies concerning the sample build direction (0°, 45°, and 90°) that were adopted in this study. Samples were soaked in a muffle furnace for 30 min at about 1050 °C, and subsequently, they were quenched in water.

For severe surface deformation, in-house developed SMAT setup was used. SMAT was carried out for 10 min using 5 mm diameter balls of high carbon steel (hardness ≈ 65 HRC). Velocity of ball in SMAT cabin was measured using a high-speed camera. The measured velocity of the ball was about

10 (± 1.2) m/s. Table 2 shows the designations of the samples used in the study. The surface roughness of samples was measured using a two-dimensional (2D) surface profilometer. The samples were cleaned using ethanol after severe surface deformation. Surface and cross-section of the samples were polished up to 5000 grade SiC emery paper, followed by fine (up to 0.25 μm) diamond paste for metallographic study.

Metallographically prepared samples (with and without etching) were investigated using an optical microscope (OM) and scanning electron microscopy (SEM). For the porosity measurement, the optical images were analysed by ImageJ software (using contrast difference method). The samples were etched (using a solution containing 5 ml HNO_3 and 15 ml HCl) for microstructural study using OM and SEM. Furthermore, electron backscatter diffraction (EBSD) was used to obtain the microstructural details like distribution of grain size, grain boundary misorientation, and geometrically necessary dislocation (GND) of annealed and severely deformed samples. For EBSD experiments, all the samples were electro-polished and EBSD maps were obtained using 20 kV accelerating voltage with 100 nm step-size.

X-ray diffraction (XRD) was carried out on the surface of heat-treated (annealed) and severely deformed samples. Cu-Kα radiation (λ = 1.5406 Å) and 2θ angle in the range of 20–90° were used to record XRD patterns.

The nanoindentation (Hysitron TI premier Nano-Indenter) using Berkovich tip (tip radius = 60 to 100 nm) was performed on the polished (surface roughness, $R_a \cong 200$ nm) cross-section of severely deformed samples to measure the hardness. The indent was taken at the normal load of 8000 μN with 5 s dwell time.

The ball-on-disc type dry reciprocating wear test was performed on non-treated and surface-treated samples at room temperature. In the wear test, sample (disc) reciprocate against alumina ball (10 mm diameter, ~1700 HV hardness, and average surface roughness (R_a) of 0.0148 ± 0.001 μm). Typically, wear behaviour of materials depends on the surface roughness [30], and therefore, to

eliminate the surface roughness factor in the tribological study of samples built in different directions, NS1, NS2, and NS3 samples were polished ($R_a \cong 0.02$ μm). The reciprocating wear test was performed using 3 Hz frequency and 4 mm sliding distance (l) for 7200 s under 5, 10, and 20 N load, and wear-rate was calculated using Eq. (1):

$$W_r = \frac{\Delta A * l}{P} \quad (1)$$

where W_r is the wear-rate (mm^3/N), P is the applied load (N), and ΔA is the cross-sectional area of the wear track, which was measured at four different locations using 2D surface profilometer (Taylor and Hobson; Software: TalyProfile Gold V7.4)). The coefficient of friction (COF) versus time was recorded during each wear test. The worn surface of the samples was studied using SEM.

3. Results and Discussion

3.1 Microstructural response of SLM 316L Stainless Steel: the Role of Build Direction

The effect of build direction on the microstructure of SLM 316L stainless steel was investigated using EBSD (Fig. 2). Figure 2(a), (d), and (g) shows IPF (inverse pole figure) maps of NS1, NS2, and NS3 samples, respectively. IPF maps show the random orientations of grains throughout the samples built in different directions. There is no indication of a specific texture for the samples, and nature of the texture is not identical for different build directions (Fig. 2(j)-(l))). The distribution of grain size is non-uniform for all samples, and it ranges from 10 to 100 μm. The average grain-size, based on high angle grain boundaries (HAGBs), is about 63, 51, and 41 μm for NS1, NS2, and NS3 samples, respectively. Due to the rapid cooling of the samples in the SLM technique, the grains are generally elongated in the laser scanning direction (SD) [31]. Figure 2(b), (e), and (h) shows the grain boundary maps of NS1, NS2, and NS3 samples, respectively. These maps are mainly dominated by HAGBs (misorientation > 15°). However, some regions have low angle grain boundaries (LAGBs) with 2°–15° misorientation. The low-angle boundaries indicate the presence of strain gradient and dislocations

in the samples [32], which are probably generated due to the rapid cooling of molten material in the SLM process. During layer-by-layer deposition in the SLM technique, shrinkage associated with the solidification of the molten pool can be constrained by the previously solidified substrate, leading to the accumulation of strain in the sample. Geometrically necessary dislocation (GND) maps reveal the domination of strain gradient along the grain boundaries, and it is somewhat more pronounced in the regions with LAGBs. NS1 sample shows more clusters of areas having lower GND as compared to NS2 and NS3 samples. In other words, NS2 and NS3 samples have more regions with higher strain. These observations suggest that the accumulation/distribution of strain in SLM AISI 316L steel is dependent on the build direction of the samples. The average density of such geometrically necessary dislocations in all samples is about 5.5×10^{13} m^{-2}, which is significantly higher than a typical annealed wrought 316L stainless steel (~10^{9} – 10^{10} m^{-2}) [33,34]. Usually, such difference in the dislocation density influences the mechanical properties of the materials such as yield strength [35-38] and hardness [11,34,39,40].

3.2 Response of SLM 316L Stainless Steel to Severe Surface Deformation

3.2.1 Effect on Macro-defects

Surface mechanical attrition treatment (SMAT) process (using 5 mm diameter hardened steel balls moving with the velocity of ~10 m/s) was used for severe surface deformation of SLM 316L steel samples. Presence of macro-defects is one of the most common problems that occur in the production of almost all metallic materials by SLM technique [11,41,42], and such problems significantly affect their mechanical properties [11,43]. Figure 3 shows the optical micrographs (without etching) of the cross-section of S1, S2, and S3 samples. The cross-section of these samples contains (i) the deformed layer near-surface and (ii) non-treated core. Core of these samples (a portion of which is indicated by dashed-rectangles in Fig. 3(a)-(c)) shows the presence of defects like lack of fusion with non-melted powder particles (locations-1 in Fig. 3(a)-(c) and Fig. 3(d)), incomplete melting-induced porosity

(locations-2 in Fig. 3(a)-(c) and Fig. 3(e)), cracks (locations-3 in Fig. 3(b)-(c) and Fig. 3(f)), and entrapped-gas porosity (Fig. 3(g)). Area fraction of such defects in the micrographs varies with the build directions, and it is about 4.23, 0.96, and 2.3% for NS1, NS2, and NS3 samples, respectively. Convincing disappearance of these defects is observed in the severely deformed layer of the samples. In short, Fig. 3 suggests that the printing of sample in a 45º build direction being beneficial in inducing lower porosity in the SLM material, and the severe surface deformation can eliminate almost all porosity in the treated layer.

3.2.2 Microstructural Response

Figure 4 shows the microstructure of the cross-section of non-treated and severely surface deformed SLM 316L steel sample manufactured in 90° direction (here, NS3/S3 sample is taken as an example to show the effect of severe deformation because other samples show the similar response). As the sample is heat-treated after additive manufacturing (Section 2), the melting pool boundaries and sub-structure boundaries are disappeared [11,38]. As mentioned above, the microstructure shows the presence of coarse and fine grains, and the grain size is ranged from about 10 to 100 μm (average grain size: 41 μm for NS3). The coarse and elongated grains (in the direction of scanning) are shown at location-A, and very fine grains are shown at location-B (Fig. 4(a)). Figure 4(b)–(d) shows the micrographs of the cross-section of the severely deformed sample. A very high density of closely spaced parallel lines (which can be called as slip bands or slip lines or deformation bands) is visible in the grains of deformed layer [44,45]. The density of slip bands decreases with increase in depth from deformed surface (up to a distance of about 600 μm for S3 sample). A magnified micrograph (Fig. 4(d)) shows intense intersections of many slips lines, which are caused due to the severe plastic deformation and low stacking fault energy (SFE) of the austenitic stainless steel [26,28]. Such response of the steel can cause nanocrystallization of the surface [45].

Figure 5 shows the EBSD results of the S3 sample. Image quality (IQ) map (Fig. 5(a)) constructed from EBSD data reveals useful information of the microstructure, where the change in colour contrast is due to the strain gradient (lattice distortion), defects, and other microstructural features. The grain boundaries and a dense network of slip bands are visible in the IQ map of the deformed layer. Figure 5(b) shows the inverse pole figure (IPF) map of the cross-section of the S3 sample. A marginal difference is observed in the average grain size (determined using an entire area of IPF map) of NS3 and S3 samples (Fig. 6(a) and (b)), where it is decreased from 40.93 μm to 38.72 μm due to the severe surface deformation. The associated pole figures indicate a random orientation of grains before and after the surface treatment (Fig. 6(c) and (d)). However, the nature of texture is not identical for the non-treated and treated samples, which indicates the possibility of a change in the orientation of grains due to the severe surface deformation. In the IPF map, diffused colour contrast within the grains suggests the presence of considerable strain and sub-division of grains by dislocations and slip bands [27,45,46].

Typically, a large deformation of conventionally manufactured austenitic stainless causes the formation of deformation-induced martensite (α'-bcc) phase [28,29,47]. However, in the current work on severely deformed SLM 316L stainless steel samples, the phase map shows a negligible quantity of α' and almost 99% austenite (γ-fcc) phase (Fig. 5(c)). The XRD results discussed in the subsequent section also reveal a similar observation. Moreover, other literature indicates such analogous behaviour in case of SLM 316L stainless steel [48,49]. Hong et al. showed that, at 10% strain, the martensitic transformation in SLM 316L stainless steel do not occur at 300 K temperature; however, a considerable quantity of martensite (about 31%) forms at 80 K temperature [50]. The pre-existence of strain gradient and inhomogeneity in the microstructure of SLM 316L make possible to resist the nucleation of α' during surface-deformation at room temperature.

Figure 5(d) shows the Kernel Average Misorientation (KAM) map, which is generally used to represent the average misorientation between a given point and its nearest neighbours that belong to

the same grain. KAM is associated with a misorientation less than 5°. Therefore, the KAM is useful to assess the local plastic strain in the sample. High KAM values are observed throughout the sample, indicating the presence of very high plastic strain in the severely deformed layer of the sample. Such plastic strain generates a high density of slip bands (Figs. 4 and 5 (a)) and dislocations (Fig. 5(e)). Figure 5(e) shows GND distribution in the surface-treated sample. SMAT process produces a large plastic strain in the material, and plastic strain is directly proportional to an average GND density [34, 35]. The average GND of NS3 sample is about 5.5×10^{13} m^{-2} (Section 3.1), and that of S3 sample is about 1.2×10^{14} m^{-2} (i.e., GND of SMAT processed sample is about 2.2 times the GND of the annealed sample).

3.2.3 Surface Roughness and XRD

Control on surface roughness is one of the major challenges in SLM materials. A rough surface is not suitable for many engineering applications because it can reduce a dimensional accuracy, generate stress concentration, accelerate crack initiation and propagation, increase corrosion rate, increase friction, and decrease wear resistance [11,17]. Figure 7(a) shows the 2D surface profiles of as-built, polished, and severely deformed sample surface. The SLM fabricated materials show very high surface roughness due to the non-melted powder and entrapment of gas on the surface [42]. The R_a value of as-built SLM 316L stainless steel is about 6.084 ± 0.003 μm, which is much larger than the polished surface (R_a = 0.020 ± 0.001 μm). In the SMAT process, a continuous bombardment of steel balls (with high velocity) decreases the R_a value by ~87% (i.e., R_a = 0.819 ± 0.002 μm, which is considerably lower than the R_a value of the as-built surface). Figure 7(b) compares the optical micrographs of the cross-section of NS3 (as-built) and S3 (surface-deformed) samples, and they endorse the smoothening of the surface due to the sever surface deformation of SLM sample.

Figure 7(c) shows the XRD patterns of NS1, NS2, and NS3 samples, and all peaks present in the XRD patterns confirm the presence of only the austenitic phase (γ-Fe) in the samples. A

considerable broadening of these peaks indicates the presence of high strain in the samples (see also Section 3.1). Figure 7(d) compares the XRD patterns of the annealed sample and severely surface deformed sample. In contrast to the typical observation associated with the severely deformed austenitic stainless steel [26,28], the current results reveal the absence of austenite to martensite transformation during deformation of SLM steel (XRD pattern of S3 sample does not show any peak corresponding to α'-bcc phase). In the higher index planes of austenite (i.e., γ(200) and γ(220)), considerable peak-broadening is observed in case of the severely deformed sample. The broadening in peaks indicates the grain refinement, misorientation, and presence of dislocations in the material [48,51,52].

3.2.4 Effect on Hardness: The Role of Build Direction and SMAT

The load-displacement curves obtained using nanoindentation at various depths from the treated-surface of S1, S2, and S3 samples are shown in Fig. 8(a)-(c). These curves follow the parabolic shape during loading (maximum load: 8000 μN). After 5 s dwell time, unloading curve shows a slight reduction in indentation depth, which occurs due to elastic recovery of the material. The maximum displacement (h_{max}) and final displacement (h_f) increase with an increase in the distance (depth) from the treated surface. Figure 8(d) shows the variation in hardness (obtained according to Oliver–Pharr analysis [53]) in the severely deformed layer of S1, S2, and S3 samples. Hardness-depth profile of S2 is above S1, and that of S3 is above S1 and S2. Improvement in the hardness of near-surface region (concerning hardness corresponding to the constant depth of 600 μm, which is much away from the surface and it is almost in the non-treated core: see Fig. 4) is about 32, 34, and 54% for the S1, S2, and S3 samples, respectively (Table 3). These observations indicate that the response of the sample to severe surface deformation depends on its build direction. Such behaviour is possible due to the variation in grain size, strain distribution, and nature of texture of the samples built in different directions (section 3.1).

Typically, the hardness of annealed austenitic stainless steel is about 3 GPa [54]. However, somewhat higher hardness of non-treated samples (Table 3) is attributed to the presence of higher dislocation density (5.5×10^{13} m^{-2}: see section 3.1). The dislocation density increases by about 2.2 times due to the severe surface deformation (section 3.2.2). Such a high density of dislocations constrains their motion, resulting in the considerable rise in the hardness of the steel [10, 11, 12, 43]. Overall, the increment in the hardness of the SMATed samples is basically due to the grain refinement, residual stress, and strain hardening (caused by the high dislocation density and formation of a dense network of slip bands) (Figs. 4-6) [26,28,54-56]. The reduced severity of surface deformation causes a gradual drop in hardness from surface to core.

3.3 Tribological Behaviour of SLM 316L Steel: The Role of Building Direction and SMAT

A dry reciprocating wear experiments were performed on the polished SLM samples ($R_a \cong 0.02$ μm: see Table 3 and Fig. 7(a)). Generally, the wear rate is highly dependent on porosity, grain orientation, surface condition, and hardness of the material [11,17,26,57,58]. The variation in wear rate with normal load is shown in Fig. 9(a) for NS1, NS2, and NS3 samples. The increase in the normal load causes an increase in wear rate which is associated to a rise in stress between the contacting surfaces [26,59,60]. It is also observed that the wear rate depends on the build direction of the sample. Such dependency on build direction is relatively lower under the lower load (5 N). The hardness alone cannot be a governing factor in wear; however, the porosity has a vital role in case of SLM samples [17]. The pores in the SLM material can act as the crack-initiation sites, leading to an increase in the volume loss of the material during dry-friction wear. Wear resistance of NS3 sample under the higher loads (especially, 20 N) is superior among the non-treated samples, which is possible due to the lower macro-defects (section 3.2.1), smallest grain size (section 3.1), and slightly higher hardness (Table 3). Figure 9(b) shows the 2D profiles across the wear tracks (which represents the cross-sections of the

worn surface) of NS1, NS2, and NS3 samples tested under 10 N load. These results show that the cross-sectional area of wear track is maximum for NS1 sample and minimum for NS3 sample.

Figure 9(c)-(e) shows the effect of severe surface deformation on the tribological response of S1, S2, and S3 samples (in comparison with the corresponding non-treated samples). The surface roughness of these samples after SMAT processing is approximately 0.8 μm (Table 3 and Fig. 7(a)-(b)). Like the non-treated samples, wear rate increases with an increase in normal load. The dependency of wear rate on load can be affected by the surface conditions (like porosity, roughness, phase transformation during wear, localized surface-heating, etc.) [26]. Wear rate of the surface-treated samples is lower than the non-treated sample under the different loads. The severe surface deformation causes an increase in the surface hardness (Fig. 8 and Table 3) and elimination of macro-defects (section 3.2.1) in the deformed layer, leading to an enhancement in the load-bearing capacity and hence, an improvement in the wear resistance [26,61]. Figure 9(f) compares the cross-sectional profiles of wear tracks for NS3 and S3 samples tested under 10 N load. The area of the cross-section of wear track generated on severely deformed samples is smaller than the corresponding non-treated sample, which signifies a lower volume loss of the surface-treated sample during wear study.

As per the Archard equation, the wear rate is inversely proportional to the hardness. Figure 10 shows the wear rate versus the surface hardness of non-SMATed and SMATed SLM 316L samples under different loading conditions. The decreasing trend of the wear rate with increase in the hardness is observed for the samples.

Figure 11 shows the results of the coefficient of frictional (COF) for the non-treated and surface-treated samples. Figure 11(a) and (b) shows the variation of COF with time, where the COF profiles can be divided into (i) running-in stage and (ii) steady-state stage. In the running-in stage, the COF increases rapidly. COF increases gradually with time in the steady-state stage. The average values of COF in the steady-state phase are plotted in Fig. 11(c)-(f) for the samples studied under different load. Except for 5 N load, NS3 sample shows the lowest COF among the non-treated samples (Fig.

11(c)), which is possible due to the slightly higher hardness and smaller grain size. The severely deformed surface shows the lower COF than the corresponding non-treated surface throughout the test duration (Fig. 11(b)) and almost under different loads (Fig. 11(d)-(f)) (except for S1 sample under 5 N load). A harder surface can exhibit a lower COF in the wear experiment [58,62,63]. Increase in load increases the COF of all samples. Complex interactions of the events like change in the hardness (domination of strain-hardening or thermal softening) and the formation of wear debris during wear test influence the COF [26].

The micrographs of worn surface of NS1, NS2, and NS3 samples are shown in Fig. 12(a), (b), and (c), respectively. The worn surface morphology of the S3 sample is shown in Fig. 12(d) as a representative of surface-deformed samples. All the samples show the presence of scratching (abrasion wear) on the worn surface. Entrapment of wear debris between the ball (counter surface) and the sample surface causes such scratching. NS1 sample shows severe scratching (due to its lower hardness). Apart from scratching, indications of delamination and adhesion are prominently visible for the non-treated samples. During the continuous sliding of the steel ball on the sample surface, the formation of cracks can occur underneath the surface, which propagate and cause delamination wear [17,26,64]. Softening of the material (due to the frictional heating) during dry sliding could be responsible for adhesion wear [26,65,66]. Due to the high hardness (Fig. 8) and low macro-defects in the severely deformed layer (Fig. 3(a)-(c)), the domination of scratching (abrasion wear) is observed on the worn surface of the surface-treated sample (Fig. 12(d)).

4. Conclusions

- The microstructure of annealed SLM 316L stainless steel samples shows a non-uniform distribution and random orientation of the grains for all build directions (0°, 45°, and 90°). High angle grain boundaries (HAGBs) dominate the microstructure. However, clusters of low angle grain boundaries (LAGBs) spread in the microstructure. The average grain size is about 63, 51,

and 41 μm for 0°, 45°, and 90° build direction, respectively. The geometrically necessary dislocation (GND) maps reveal the uneven distribution of strain gradient within the specimens. The average density of GND in the annealed SLM steel samples is about 5.5×10^{13} m^{-2}, which is significantly higher than a typical annealed wrought stainless steel. Samples manufactured in 45° and 90° directions have a slightly higher density (i.e., lesser macro-defects) than the sample having 0° build direction.

- Severe surface deformation (as a post-treatment) of the SLM 316L stainless steel is beneficial to reduce the surface roughness (by ~87%) and eliminate internal porosity in the deformed layer.
- Due to the application of severe surface deformation (using SMAT process), a highly dense network of slip bands is generated (up to a depth of about 600 μm) in the deformed layer. The average dislocation density of severely deformed layer is about 2.2 times higher than that of the annealed sample. Increase in surface hardness due to the SMAT is maximum (~54%) for the sample manufactured in 90° build direction. Severe surface deformation of SLM 316L steel does not cause the formation of deformation-induced martensite.
- In dry reciprocating wear study, wear rate of annealed samples and surface-treated samples is increased with an increase in the normal load (from 5 to 20 N). In the case of annealed samples (without surface treatment), wear rate and COF are independent of build direction under the lower load (5 N). However, under the higher load (especially, 20 N), wear-resistance and COF of sample manufactured in 90° build direction are superior amongst the non-treated samples. SMAT process enhances the wear resistance and reduces the COF of SLM steel.

Acknowledgments:

The authors would like to thank SERB [grant number EMR/2017/001196] for their support for this research. The nanoindentation and EBSD facilities of IIT Bombay are kindly acknowledged.

References:

1. Q. Chen, G.A. Thouas, Metallic Implant Biomaterials, *Materials Science and Engineering: R: Reports*, **87**, 1-57 (2015)
2. Y. Zhang, F. Liu, J. Chen, Y. Yuan, Effects of Surface Quality on Corrosion Resistance of 316L Sainless Steel Parts Manufactured via SLM, *Journal of Laser Applications*, **29**(2), 022306 (2017)
3. K. Saeidi, M. Neikter, J. Olsen, Z.J. Shen, F. Akhtar, 316L Stainless Steel Designed to Withstand Intermediate Temperature, *Materials & Design*, **135**, 1-8 (2017)
4. W.J. Oh, W.J. Lee, M.S. Kim, J.B. Jeon, D.S. Shim, Repairing Additive-Manufactured 316L Stainless Steel Using Direct Energy Deposition, *Optics & Laser Technology*, **117**, 6-17 (2019)
5. J. Kranz, D. Herzog, C. Emmelmann, Design Guidelines for Laser Additive Manufacturing of Lightweight Structures in TiAl6V4, *Journal of Laser Applications*, **27**(S1), S14001 (2015)
6. K. Wong, A. Hernandez, A Review of Additive Manufacturing, ISRN Mechanical Engineering, 2012, *DOI http://dx.doi.org/10.5402/2012/208760*,
7. E. Liverani, S. Toschi, L. Ceschini, A. Fortunato, Effect of Selective Laser Melting (SLM) Process Parameters on Microstructure and Mechanical Properties of 316L Austenitic Stainless Steel, *Journal of Materials Processing Technology*, **249**, 255-263 (2017)
8. J. Liu, Y. Song, C. Chen, X. Wang, H. Li, J. Wang, K. Guo, J. Sun, Effect of Scanning Speed on the Microstructure and Mechanical Behavior of 316L Stainless Steel Fabricated by Selective Laser Melting, *Materials & Design*, **186**, 108355 (2020)
9. L. Zheng, Y. Liu, S. Sun, H. Zhang, Selective Laser Melting of Al–8.5 Fe–1.3 V–1.7 Si Alloy: Investigation on the Resultant Microstructure and Hardness, *Chinese Journal of Aeronautics*, **28**(2), 564-569 (2015)
10. D. Herzog, V. Seyda, E. Wycisk, C. Emmelmann, Additive Manufacturing of Metals, *Acta Materialia*, **117**, 371-392 (2016)
11. E. Tascioglu, Y. Karabulut, Y. Kaynak, Influence of Heat Treatment Temperature on the Microstructural, Mechanical, and Wear Behavior of 316L Stainless Steel Fabricated by Laser Powder Bed Additive Manufacturing, *The International Journal of Advanced Manufacturing Technology*, 1-10 (2020)
12. K. Saeidi, X. Gao, Y. Zhong, Z.J. Shen, Hardened Austenite Steel with Columnar Sub-grain Structure Formed by Laser Melting, *Materials Science and Engineering: A*, **625**, 221-229 (2015)
13. S.M. Yusuf, Y. Chen, R. Boardman, S. Yang, N. Gao, Investigation on Porosity and Microhardness of 316L Stainless Steel Fabricated by Selective Laser Melting, *Metals*, **7**(2), 64 (2017)

14. F. Bartolomeu, M. Buciumeanu, E. Pinto, N. Alves, O. Carvalho, F. Silva, G. Miranda, 316L stainless steel mechanical and tribological behavior—A comparison between selective laser melting, hot pressing and conventional casting, *Additive Manufacturing*, 16, 81-89 (2017)
15. C. Qiu, C. Panwisawas, M. Ward, H.C. Basoalto, J.W. Brooks, M.M. Attallah, On the Role of Melt Flow Into the Surface Structure and Porosity Development During Selective Laser Melting, *Acta Materialia*, 96, 72-79 (2015)
16. G. Kasperovich, J. Haubrich, J. Gussone, G. Requena, Correlation Between Porosity and Processing Parameters in TiAl6V4 Produced by Selective Laser Melting, *Materials & Design*, 105, 160-170 (2016)
17. Y. Sun, A. Moroz, K. Alrbaey, Sliding Wear Characteristics and Corrosion Behaviour of Selective Laser Melted 316L Stainless Steel, *Journal of Materials Engineering and Performance*, 23(2), 518-526 (2014)
18. M.M. Dewidar, K.A. Khalil, J. Lim, Processing and Mechanical Properties of Porous 316L Stainless Steel for Biomedical Applications, *Transactions of Nonferrous Metals Society of China*, **17**(3), 468-473 (2007)
19. E. Yasa, J.-P. Kruth, Microstructural Investigation of Selective Laser Melting 316L Stainless Steel Parts Exposed to Laser Re-melting, *Procedia Engineering*, **19**, 389-395 (2011)
20. R. Casati, J. Lemke, M. Vedani, Microstructure and Fracture Behavior of 316L Austenitic Stainless Steel Produced by Selective Laser Melting, *Journal of Materials Science & Technology*, **32**(8), 738-744 (2016)
21. Z. Baicheng, L. Xiaohua, B. Jiaming, G. Junfeng, W. Pan, S. Chen-nan, N. Muiling, Q. Guojun, W. Jun, Study of Selective Laser Melting (SLM) Inconel 718 Part Surface Improvement by Electrochemical Polishing, *Materials & Design*, **116**, 531-537 (2017)
22. V.S. Thakur, M. Manikandan, S. Singh, S. Mishra, A. Kaithwas, S.M. Prabu, I. Palani, Laser Polishing of Wire Arc Additive Manufactured SS316L, Advances in Additive Manufacturing and Joininged., Springer, 2020, p 127-135
23. A. Amanov, Effect of Local Treatment Temperature of Ultrasonic Nanocrystalline Surface Modification on Tribological Behavior and Corrosion Resistance of Stainless Steel 316L Produced by Selective Laser Melting, *Surface and Coatings Technology*, **398**, 126080 (2020)
24. K. Lu, J. Lu, Nanostructured Surface Layer on Metallic Materials Induced by Surface Mechanical Attrition Treatment, *Materials Science and Engineering: A*, **375**, 38-45 (2004)
25. N. Tao, Z. Wang, W. Tong, M. Sui, J. Lu, K. Lu, An Investigation of Surface Nanocrystallization Mechanism in Fe Induced by Surface Mechanical Attrition Treatment, *Acta Materialia*, **50**(18), 4603-4616 (2002)

26. M.D. Joshi, V. Kumar, I. Singh, S.S. Hosmani, Tribological Response of Mechanical Attrition Treated Surface of AISI 316L Steel: The Role of Velocity of Colliding Balls, *Journal of Tribology*, **143**(3), (2020)
27. Z. Sun, D. Retraint, T. Baudin, A.-L. Helbert, F. Brisset, M. Chemkhi, J. Zhou, P. Kanouté, Experimental Study of Microstructure Changes due to Low Cycle Fatigue of a Steel Nanocrystallised by Surface Mechanical Attrition Treatment (SMAT), *Materials Characterization*, **124**, 117-121 (2017)
28. D. Singh, D.A. Basha, A. Singh, R.S. Devan, S.S. Hosmani, Microstructural and Passivation Response of Severely Deformed AISI 304 Steel Surface: The Role of Surface Mechanical Attrition Treatment, *Journal of Materials Engineering and Performance*, 1-14 (2020)
29. M.D. Joshi, V. Kumar, A.K. Litoria, D. Singh, S.S. Hosmani, Effect of Surface Mechanical Attrition Treatment on Tribological Behavior of AISI 2205 Steel, *Materials Today: Proceedings*, (2020)
30. R.A. Al-Samarai, K.R.A. Haftirman, Y. Al-Douri, The Influence of Roughness on the Wear and Friction Coefficient Under Dry and Lubricated Sliding, *Int. J. Sci. Eng. Res*, **3**(4), 1-6 (2012)
31. P.A. Hooper, Melt Pool Temperature and Cooling Rates in Laser Powder Bed Fusion, *Additive Manufacturing*, **22**, 548-559 (2018)
32. X. Huang, Characteristic Structures and Properties of Nanostructured Metals Prepared by Plastic Deformation, Nanostructured Metals and Alloys., Elsevier, 2011, p 276-295
33. S. Gorsse, C. Hutchinson, M. Gouné, R. Banerjee, Additive Manufacturing of Metals: A Brief Review of the Characteristic Microstructures and Properties of Steels, Ti-6Al-4V and High-Entropy Alloys, *Science and Technology of Advanced Materials*, **18**(1), 584-610 (2017)
34. Z. Sun, X. Tan, S.B. Tor, W.Y. Yeong, Selective Laser Melting of Stainless Steel 316L with Low Porosity and High Build rates, *Materials & Design*, **104**, 197-204 (2016)
35. T. Kurzynowski, K. Gruber, W. Stopyra, B. Kuźnicka, E. Chlebus, Correlation Between Process Parameters, Microstructure and Properties of 316 L Stainless Steel Processed by Selective Laser Melting, *Materials Science and Engineering: A*, **718**, 64-73 (2018)
36. Z. Liu, D. Zhang, S. Sing, C. Chua, L. Loh, Interfacial Characterization of SLM Parts in Multi-Material Processing: Metallurgical Diffusion Between 316L Stainless Steel and C18400 Copper Alloy, *Materials Characterization*, **94**, 116-125 (2014)
37. J. Suryawanshi, K. Prashanth, U. Ramamurty, Mechanical Behavior of Selective Laser Melted 316L Stainless Steel, *Materials Science and Engineering: A*, **696**, 113-121 (2017)

38. C. Qiu, M. Al Kindi, A.S. Aladawi, I. Al Hatmi, A Comprehensive Study on Microstructure and Tensile Behaviour of a Selectively Laser Melted Stainless Steel, *Scientific Reports*, **8**(1), 1-16 (2018)
39. M.L. Montero-Sistiaga, M. Godino-Martinez, K. Boschmans, J.-P. Kruth, J. Van Humbeeck, K. Vanmeensel, Microstructure Evolution of 316L Produced by HP-SLM (High Power Selective Laser Melting), *Additive Manufacturing*, **23**, 402-410 (2018)
40. W.M. Tucho, V.H. Lysne, H. Austbø, A. Sjolyst-Kverneland, V. Hansen, Investigation of Effects of Process Parameters on Microstructure and Hardness of SLM Manufactured SS316L, *Journal of Alloys and Compounds*, **740**, 910-925 (2018)
41. A. Sola, A. Nouri, Microstructural porosity in additive manufacturing: The Formation and Detection of Pores in Metal Parts Fabricated by Powder Bed Fusion, *Journal of Advanced Manufacturing and Processing*, **1**(3), e10021 (2019)
42. T. Ronneberg, C.M. Davies, P.A. Hooper, Revealing Relationships Between Porosity, Microstructure and Mechanical Properties of Laser Powder Bed Fusion 316L Stainless Steel Through Heat Treatment, *Materials & Design*, **189**, 108481 (2020)
43. C. Tian, X. Li, H. Li, G. Guo, L. Wang, Y. Rong, The Effect of Porosity on the Mechanical Property of Metal-Bonded Diamond Grinding Wheel Fabricated by Selective Laser Melting (SLM), *Materials Science and Engineering: A*, **743**, 697-706 (2019)
44. P. Villechaise, L. Sabatier, J. Girard, On Slip Band Features and Crack Initiation in Fatigued 316L Austenitic Stainless Steel: Part 1: Analysis by Electron Back-Scattered Diffraction and Atomic Force Microscopy, *Materials Science and Engineering: A*, **323**(1-2), 377-385 (2002)
45. G. Liu, J. Lu, K. Lu, Surface Nanocrystallization of 316L Stainless Steel Induced by Ultrasonic Shot Peening, *Materials Science and Engineering: A*, **286**(1), 91-95 (2000)
46. A. Shugurov, A. Panin, A. Dmitriev, A. Nikonov, The Effect of Crystallographic Grain Orientation of Polycrystalline Ti on Ploughing Under Scratch Testing, *Wear*, **408**, 214-221 (2018)
47. H. Huang, Z. Wang, J. Lu, K. Lu, Fatigue Behaviors of AISI 316L Stainless Steel With a Gradient Nanostructured Surface Layer, *Acta Materialia*, **87**, 150-160 (2015)
48. S.M. Yusuf, Y. Chen, S. Yang, N. Gao, Microstructural Evolution and Strengthening of Selective Laser Melted 316L Stainless Steel Processed by High-Pressure Torsion, *Materials Characterization*, **159**, 110012 (2020)
49. A. Kundu, D.P. Field, P.C. Chakraborti, Influence of Strain Amplitude on the Development of Dislocation Structure During Cyclic Plastic Deformation of 304 LN Austenitic Stainless Steel, *Materials Science and Engineering: A*, **762**, 138090 (2019)

50. Y. Hong, C. Zhou, Y. Zheng, L. Zhang, J. Zheng, X. Chen, B. An, Formation of Strain-Induced Martensite in Selective Laser Melting Austenitic Stainless Steel, *Materials Science and Engineering: A*, **740**, 420-426 (2019)
51. T. Ungar, Microstructural Parameters from X-ray Diffraction Peak Broadening, *Scripta Materialia*, **51**(8), 777-781 (2004)
52. M. Pham, B. Dovgyy, P. Hooper, Twinning Induced Plasticity in Austenitic Stainless Steel 316L Made by Additive Manufacturing, *Materials Science and Engineering: A*, **704**, 102-111 (2017)
53. W.C. Oliver, G.M. Pharr, Measurement of Hardness and Elastic Modulus by Instrumented Indentation: Advances in Understanding and Refinements to Methodology, *Journal of Materials Research*, **19**(1), 3-20 (2004)
54. Y. Wu, B. Guelorget, Z. Sun, R. Déturche, D. Retraint, Characterization of Gradient Properties Generated by SMAT for a Biomedical Grade 316L Stainless Steel, *Materials Characterization*, **155**, 109788 (2019)
55. R. Ji, Y. Liu, S. To, H. Jin, W.S. Yip, Z. Yang, C. Zheng, B. Cai, Efficient Fabrication of Gradient Nanostructure Layer on Surface of Commercial Pure Copper by Coupling Electric Pulse and Ultrasonics Treatment, *Journal of Alloys and Compounds*, **764**, 51-61 (2018)
56. F. Yan, B. Zhang, H. Wang, N. Tao, K. Lu, Nanoindentation Characterization of Nano-Twinned Grains in an Astenitic Stainless Steel, *Scripta Materialia*, **112**, 19-22 (2016)
57. P. Seenuvasaperumal, K. Doi, D.A. Basha, A. Singh, A. Elayaperumal, K. Tsuchiya, Wear Behavior of HPT Processed UFG AZ31B Magnesium Alloy, *Materials Letters*, **227**, 194-198 (2018)
58. R. Ji, Z. Yang, H. Jin, Y. Liu, H. Wang, Q. Zheng, W. Cheng, B. Cai, X. Li, Surface Nanocrystallization and Enhanced Surface Mechanical Properties of Nickel-Based Superalloy by Coupled Electric Pulse and Ultrasonic Treatment, *Surface and Coatings Technology*, **375**, 292-302 (2019)
59. X. Li, Q. Zhang, Y. Zhou, J. Liu, K. Chen, S. Wang, Mild and Severe Wear of Titanium Alloys, *Tribology Letters*, **61**(2), 14 (2016)
60. K. Farokhzadeh, A. Edrisy, Transition Between Mild and Severe Wear in Titanium Alloys, *Tribology International*, **94**, 98-111 (2016)
61. D. Jeong, F. Gonzalez, G. Palumbo, K. Aust, U. Erb, The Effect of Grain Size on the Wear Properties of Electrodeposited Nanocrystalline Nickel Coatings, *Scripta Materialia*, **44**(3), 493-499 (2001)
62. R. Mishra, B. Basu, R. Balasubramaniam, Effect of Grain Size on the Tribological Behavior of Nanocrystalline Nickel, *Materials Science and Engineering: A*, **373**(1-2), 370-373 (2004)

63. M. Guo-zheng, X. Bin-shi, W. Hai-dou, S. Hong-juan, Y. Da-xiang, Effect of Surface Nanocrystallization on the Tribological Properties of 1Cr18Ni9Ti Stainless Steel, *Mater. Lett*, (2011)
64. N.P. Suh, An overview of the Delamination Theory of Wear, *Wear*, **44**(1), 1-16 (1977)
65. K.C. Bae, K.S. Ha, Y.H. Kim, J.-J. Oak, W. Lee, Y.H. Park, Building Direction Dependence of Wear Resistance of Selective Laser Melted AISI 316L Stainless Steel Under High-Speed Tribological Environment,
66. M. Zandrahimi, A. Poladi, J.A. Szpunar, The Formation of Martensite During Wear of AISI 304 Stainless Steel, *Wear*, **263**(1-6), 674-678 (2007)

Table 1. Chemical composition of the AISI 316L stainless steel manufactured using SLM technique

Element	C	Cr	Ni	Mn	Mo	Si	P	S	N	Fe
Wt.%	≤ 0.03	16-18	10-14	≤ 2	2-3	≤ 2	≤ 0.045	≤ 0.03	≤ 0.1	Balance

Table 2. Designations of the SLM 316L stainless steel samples used in the study

Sample designation	**NS1**	**NS2**	**NS3**	**S1**	**S2**	**S3**
Building direction	0°	45°	90°	0°	45°	90°
Sample condition	Heat Treated (Annealed)			Severely Deformed Surface		

Table 3. Surface roughness (R_a), porosity, and hardness of the samples

Sample	NS1	NS2	NS3	S1	S2	S3
R_a (µm) – Surface (without polishing)	6.097	6.123	6.084	0.786	0.854	0.819
R_a (µm) – Polished surface	0.018	0.022	0.019	--	--	--
Porosity (%)	4.23	0.96	2.30	0.70 (up to 600 µm)	0.12 (up to 600 µm)	0.14 (up to 600 µm)
Surface hardness (GPa)	3.7	4.1	4.1	4.9	5.5	6.3

Fig. 1: Schematic diagrams depicting the laser scanning strategies used in the manufacturing of SLM 316L stainless steel samples

Fig. 2: Inverse pole figure (IPF), boundary misorientation, and geometrically necessary dislocation (GND) maps for (a)-(c) NS1, (d)-(f) NS2, and (g)-(i) NS3 samples. Pole figures for (j) NS1, (k) NS2, and (l) NS3 samples

Fig. 3: Optical micrographs (without etching) of the cross-section of (a) S1, (b) S2, and (c) S3 samples. (d)-(g) SEM micrographs that show the magnified view of macro-defects present in the non-treated core of the samples

Fig. 4: Optical micrographs of the etched cross-section of (a) annealed and (b) SMAT processed (i.e., severely surface deformed) SLM 316L stainless steel sample. (c)-(d) SEM micrographs of the cross-section of the severely surface deformed sample

Fig. 5: EBSD results of severely surface deformed (S3) sample: (a) image quality (IQ), (b) inverse-pole figure (IPF), (c) phase distribution, (d) Kernel Average Misorientation (KAM), and (e) geometrically necessary dislocation (GND) maps

Fig. 6: Distribution of grain size for (a) NS3 and (b) S3 samples. Comparison of pole figures for (c) NS3 and (d) S3 samples

Fig. 7: (a) 2D surface profiles of as-built, polished, and severely surface deformed SLM 316L stainless steel sample (S3). (b) Comparison of cross-sections of NS3 and S3 samples. X-ray diffraction patterns of (c) NS1, NS2, and NS3 samples, and (d) S3 vs. NS3 samples

Fig. 8: Load–displacement (P–h) curves obtained using nanoindentation at various depths from the treated-surface of (a) S1, (b) S2, and (c) S3 samples. (d) Nano-hardness depth profiles of S1, S2, and S3 samples

Fig. 9: (a) Wear rate vs. load for NS1, NS2, and NS3 samples. (b) 2D surface profiles across the wear tracks of NS1, NS2, and NS3 samples. Comparison of wear rate of non-treated and surface-treated

samples under different load: (c) NS1 vs. S1, (d) NS2 vs. S2, and (e) NS3 vs. S3. (f) 2D surface profiles across the wear tracks of NS3 and S3 samples

Fig. 10: Wear rate vs. surface hardness of non-SMATed and SMATed SLM 316L samples under different loading conditions

Fig. 11: Variation of COF with time for (a) NS1, NS2, and NS3 samples, and (b) NS3 vs. S3 samples. (c) Variation of average COF with applied load for NS1, NS2, and NS3 samples. Comparison of average COF of non-treated and surface-treated samples under different load: (d) NS1 vs. S1, (e) NS2 vs. S2, and (f) NS3 vs. S3

Fig. 12: SEM micrographs of the worn surface of (a) NS1, (b) NS2, (c) NS3, and (d) S3 samples tested under 10 N load and 3 Hz frequency (in dry reciprocating wear study)

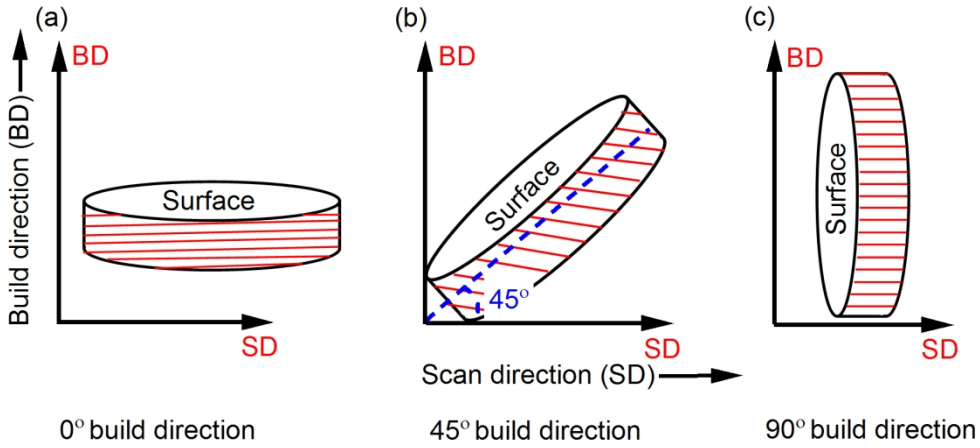

Fig. 1: Schematic diagrams depicting the laser scanning strategies used in the manufacturing of SLM 316L stainless steel samples.

157x72mm (300 x 300 DPI)

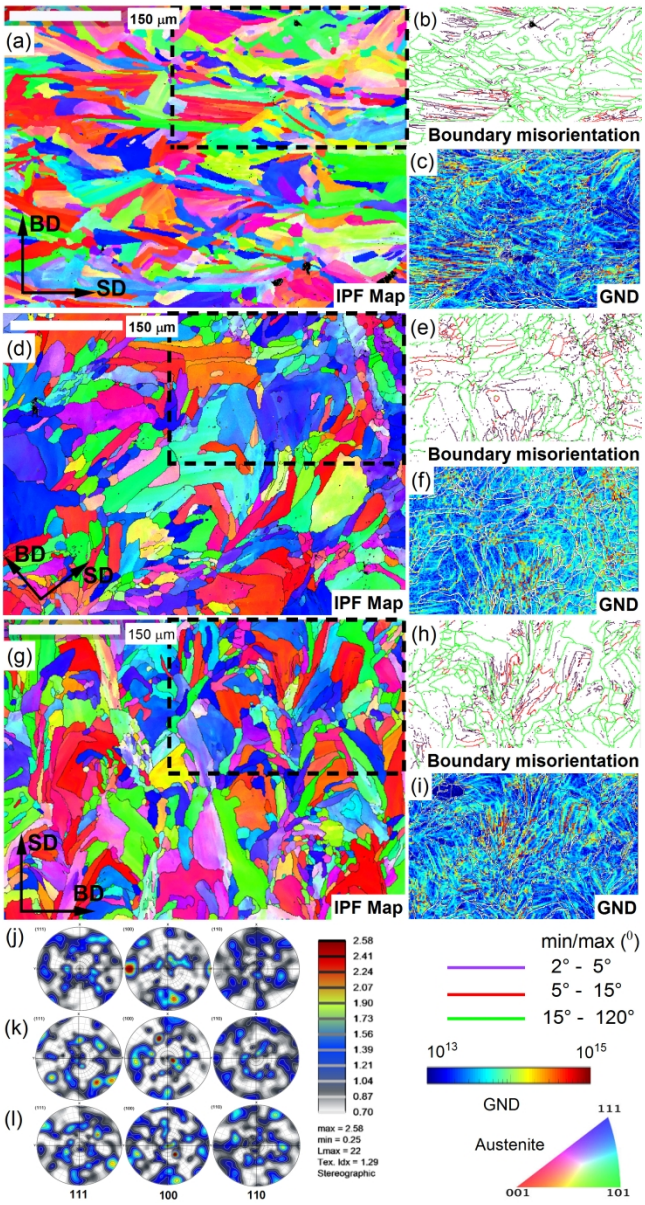

Fig. 2: Inverse pole figure (IPF), boundary misorientation, and geometrically necessary dislocation (GND) maps for (a)-(c) NS1, (d)-(f) NS2, and (g)-(i) NS3 samples. Pole figures for (j) NS1, (k) NS2, and (l) NS3 samples.

162x304mm (300 x 300 DPI)

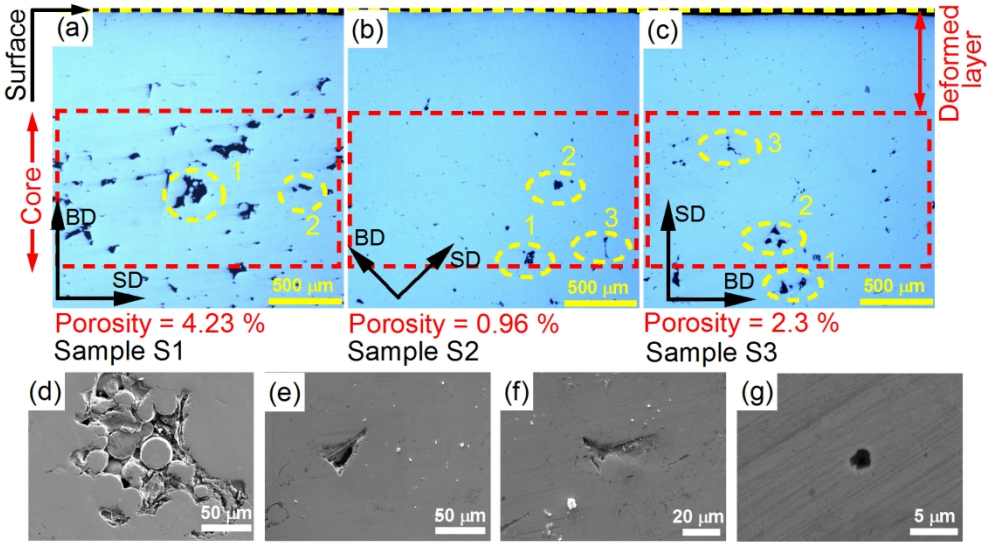

Fig. 3: Optical micrographs (without etching) of the cross-section of (a) S1, (b) S2, and (c) S3 samples. (d)-(g) SEM micrographs that show the magnified view of macro-defects present in the non-treated core of the samples.

157x88mm (300 x 300 DPI)

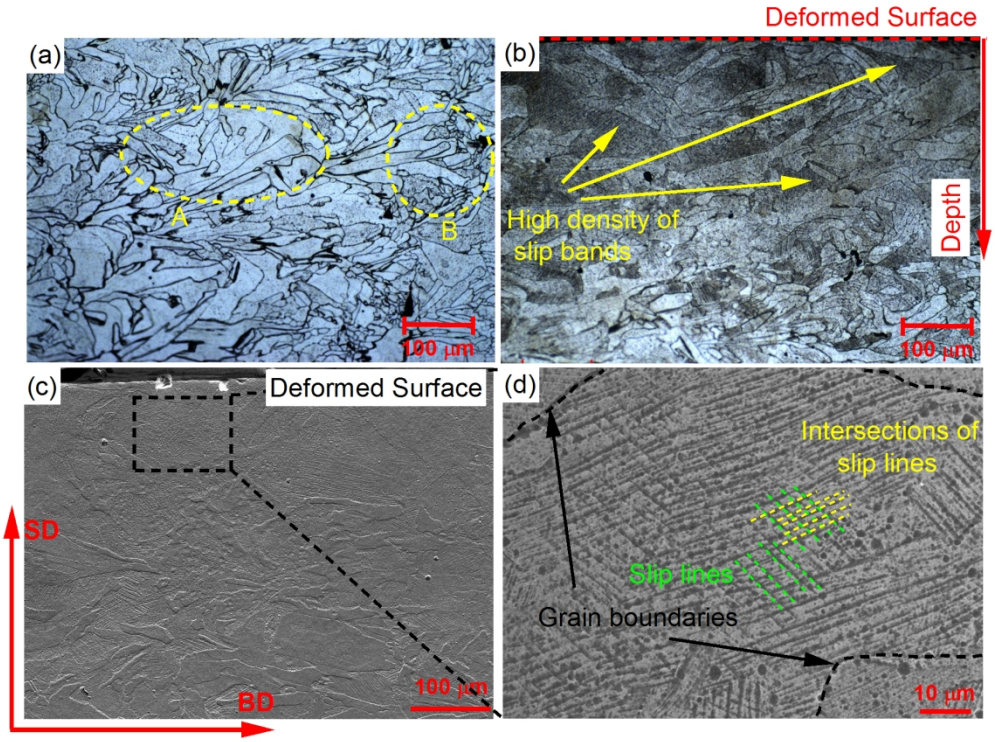

Fig. 4: Optical micrographs of the etched cross-section of (a) annealed and (b) SMAT processed (i.e., severely surface deformed) SLM 316L stainless steel sample. (c)-(d) SEM micrographs of the cross-section of the severely surface deformed sample.

162x121mm (300 x 300 DPI)

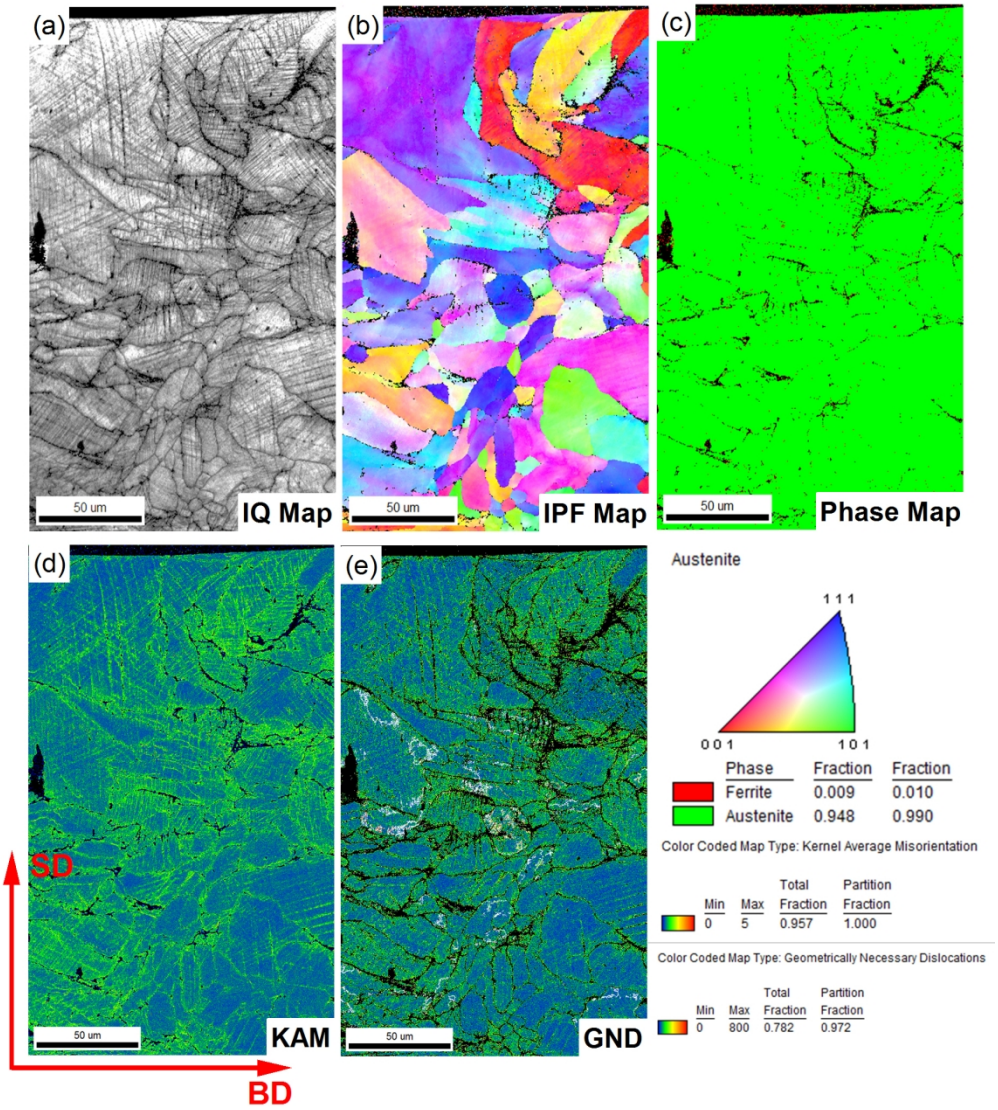

Fig. 5: EBSD results of severely surface deformed (S3) sample: (a) image quality (IQ), (b) inverse-pole figure (IPF), (c) phase distribution, (d) Kernel Average Misorientation (KAM), and (e) geometrically necessary dislocation (GND) maps.

157x178mm (300 x 300 DPI)

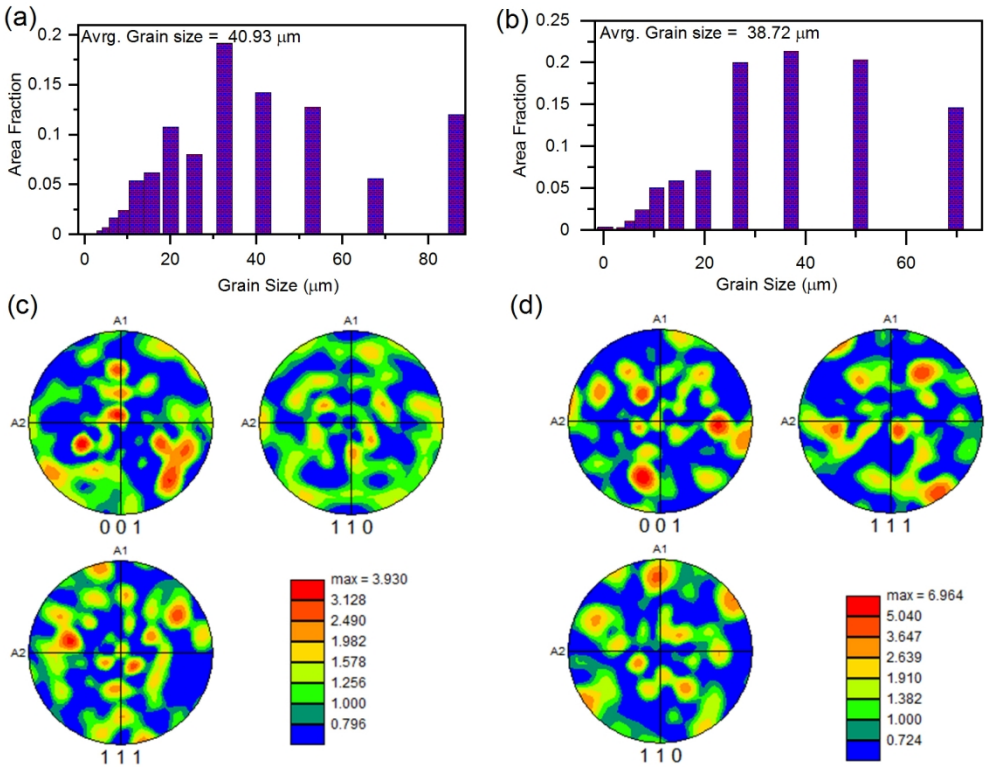

Fig. 6: Distribution of grain size for (a) NS3 and (b) S3 samples. Comparison of pole figures for (c) NS3 and (d) S3 samples.

157x120mm (300 x 300 DPI)

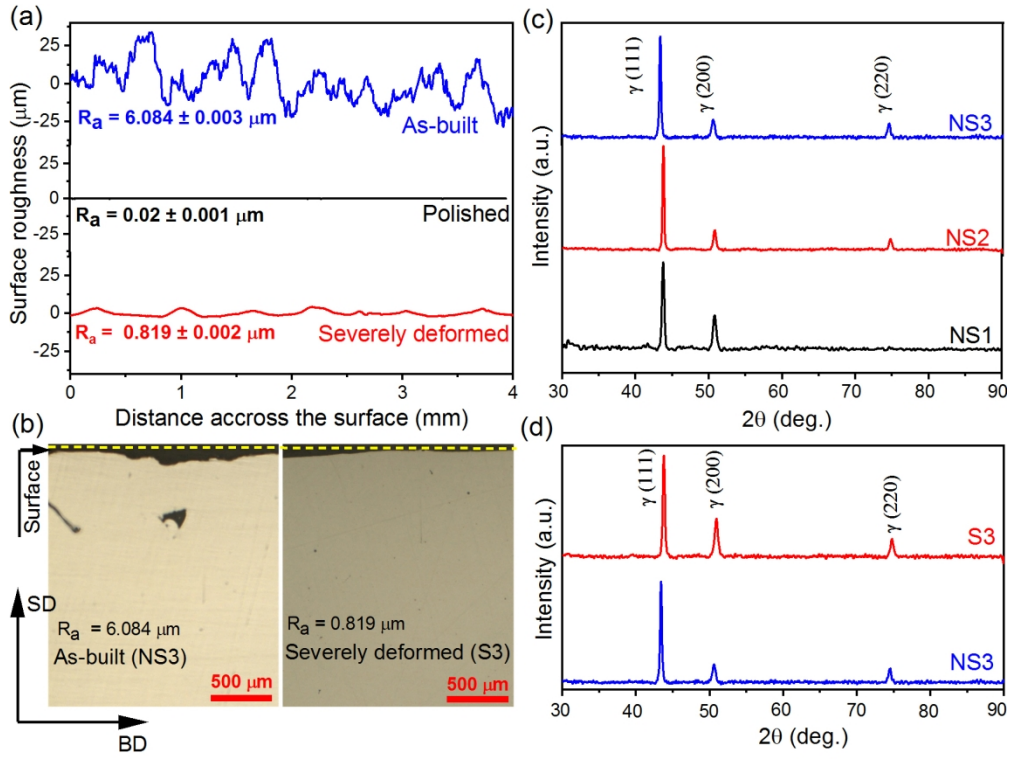

Fig. 7: (a) 2D surface profiles of as-built, polished, and severely surface deformed SLM 316L stainless steel sample (S3). (b) Comparison of cross-sections of NS3 and S3 samples. X-ray diffraction patterns of (c) NS1, NS2, and NS3 samples, and (d) S3 vs. NS3 samples.

157x123mm (300 x 300 DPI)

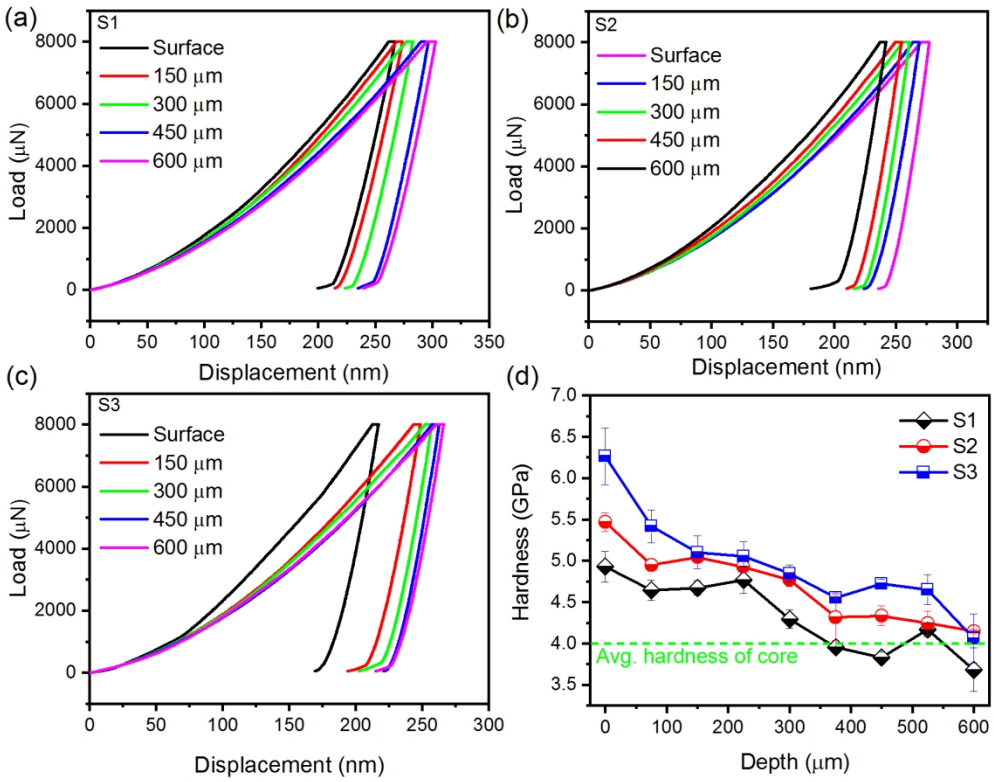

Fig. 8: Load–displacement (P–h) curves obtained using nanoindentation at various depths from the treated-surface of (a) S1, (b) S2, and (c) S3 samples. (d) Nano-hardness depth profiles of S1, S2, and S3 samples.

157x124mm (300 x 300 DPI)

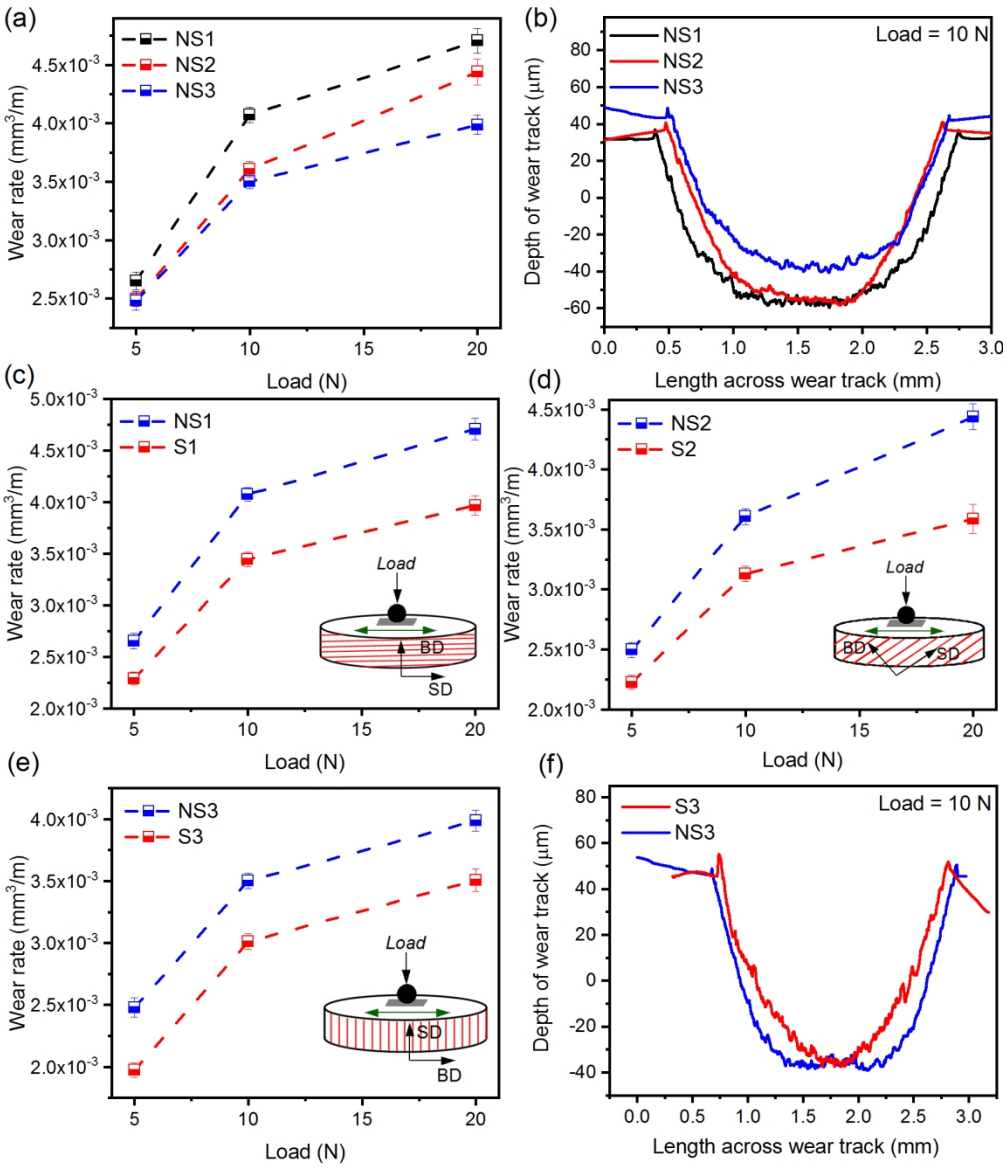

Fig. 9: (a) Wear rate vs. load for NS1, NS2, and NS3 samples. (b) 2D surface profiles across the wear tracks of NS1, NS2, and NS3 samples. Comparison of wear rate of non-treated and surface-treated samples under different load: (c) NS1 vs. S1, (d) NS2 vs. S2, and (e) NS3 vs. S3. (f) 2D surface profiles across the wear tracks of NS3 and S3 samples.

157x183mm (300 x 300 DPI)

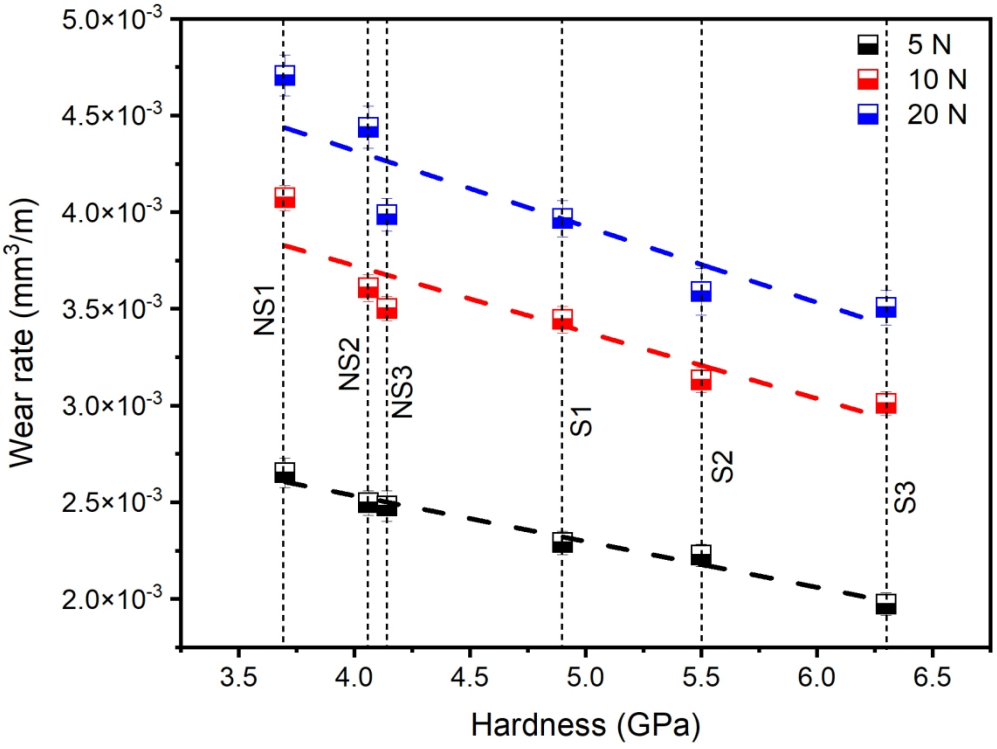

Fig. 10: Wear rate vs. surface hardness of non-SMATed and SMATed SLM 316L samples under different loading conditions.

155x116mm (300 x 300 DPI)

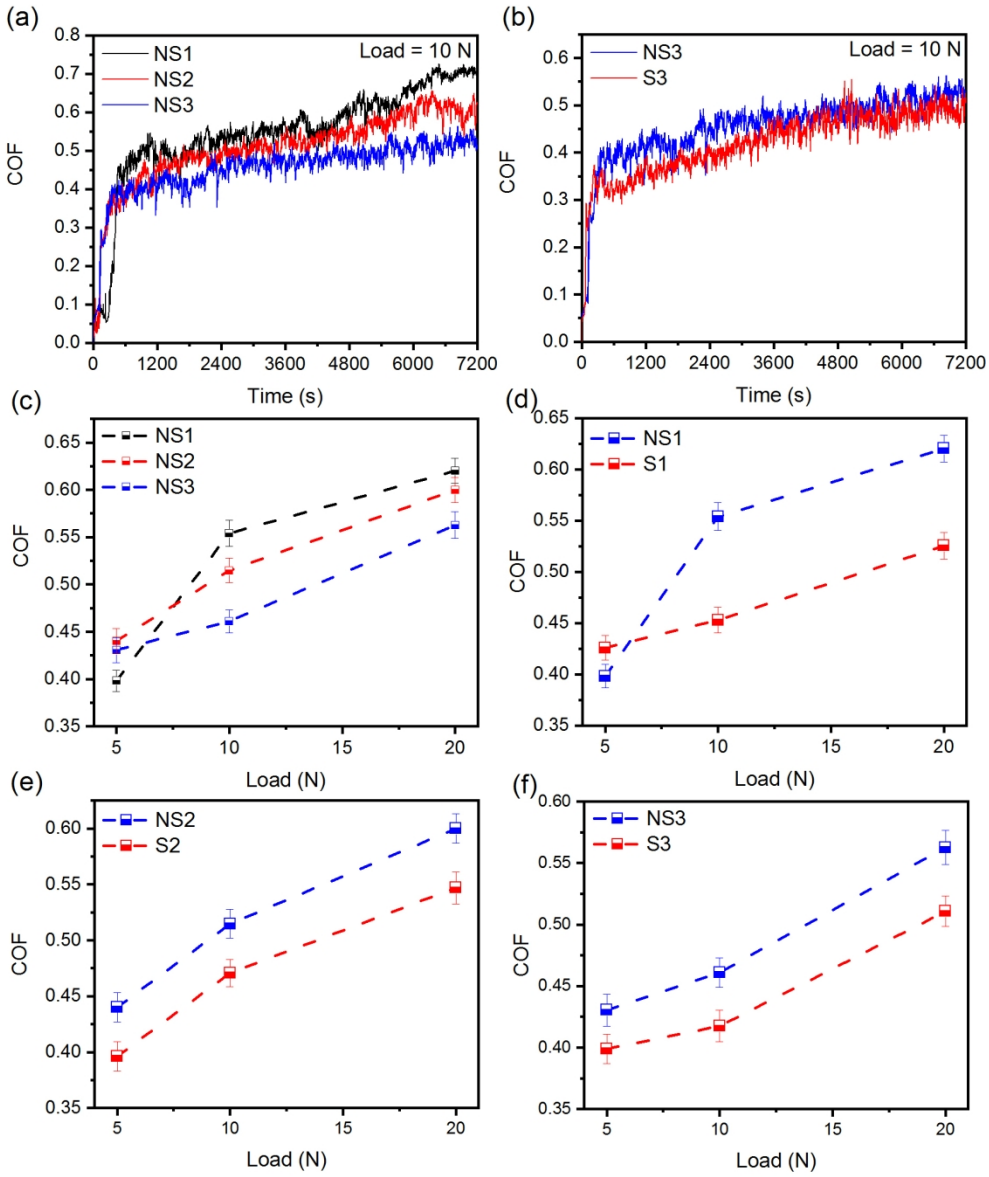

Fig. 11: Variation of COF with time for (a) NS1, NS2, and NS3 samples, and (b) NS3 vs. S3 samples. (c) Variation of average COF with applied load for NS1, NS2, and NS3 samples. Comparison of average COF of non-treated and surface-treated samples under different load: (d) NS1 vs. S1, (e) NS2 vs. S2, and (f) NS3 vs. S3.

157x190mm (300 x 300 DPI)

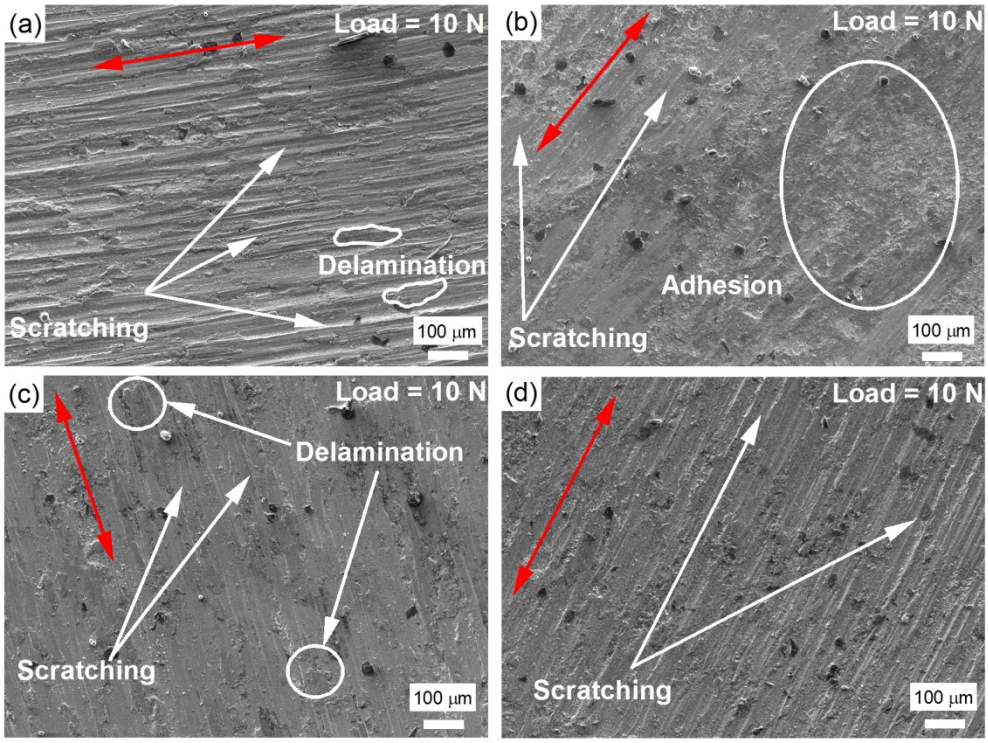

Fig. 12: SEM micrographs of the worn surface of (a) NS1, (b) NS2, (c) NS3, and (d) S3 samples tested under 10 N load and 3 Hz frequency (in dry reciprocating wear study).

157x119mm (300 x 300 DPI)